Monte Carlo simulations and mean-field modeling of electric double layers at weakly and moderately charged spherical macroions

Daniel L. Z. Caetano ⬤

Institute of Chemistry, State University of Campinas (UNICAMP), Campinas, São Paulo 13083-970, Brazil
and Center for Computational Engineering and Sciences, State University of Campinas (UNICAMP), Campinas, São Paulo 13083-970, Brazil

Sidney J. de Carvalho ⬤ and Guilherme V. Bossa ⬤*

Department of Physics, São Paulo State University (UNESP), Institute of Biosciences,
Humanities and Exact Sciences, São José do Rio Preto, São Paulo 15054-000, Brazil

Sylvio May ⬤

Department of Physics, North Dakota State University, Fargo, North Dakota 58108, USA

Monte Carlo simulations are employed to determine the differential capacitance of an electric double layer formed by small size-symmetric anions and cations in the vicinity of weakly to moderately charged macroions. The influence of interfacial curvature is deduced by investigating spherical macroions, ranging from flat to moderately curved. We also calculate the differential capacitance using a previously developed mean-field model where, in addition to electrostatic interactions, the excluded volumes of the ions are taken into account using either the lattice-gas or the Carnahan-Starling equation of state. For both equations of state, we compare the mean-field model for arbitrary curvature with a recently developed second-order curvature expansion. Our Monte Carlo simulations predict an increase in the differential capacitance with growing macroion curvature if the surface charge density is small, whereas for moderately charged macroions the differential capacitance passes through a local minimum. Both mean-field models tend to somewhat overestimate the differential capacitance as compared with Monte Carlo simulations. At the same time, they do reproduce the curvature dependence of the differential capacitance, especially for small surface charge density. Our study suggests that the quality of mean-field modeling does not worsen when weakly or moderately charged macroions exhibit spherical curvature.

I. INTRODUCTION

A charged macroion immersed in a salt-containing aqueous solution induces the formation of an electric double layer (EDL). EDLs continue to attract interest not only because of their omnipresence in all living cells, but also due to emerging technological applications such as in water desalination [1,2], oil extraction from porous rocks [3], and energy storage devices [4–13]. The ability of EDLs to store energy, for instance, has received growing attention due to the improvement in the design of supercapacitors which, besides the greater life cycle, offer an environment-friendly alternative to conventional batteries. More precisely, theoretical [14–19] and experimental [7,9,20–22] studies suggest that the energy density of supercapacitors can be increased by using nanostructured microporous electrodes based on carbide-derived materials [23–28]. Generally, the ability of an EDL to store energy is manifested by the differential capacitance C_{diff}, which expresses the relationship between electrostatic potential and charge density on the surface of an electrified interface. Being an experimentally accessible property that reflects the microscopic structure of the EDL [5,16,29,30],

the differential capacitance C_{diff} serves as a meaningful link between experimental, theoretical, and simulation work for all EDLs.

Most previous theoretical models for C_{diff} have focused on planar macroions because this geometry offers mathematical simplicity. Recent modeling efforts have included the dependence of EDL properties on macroion geometry, including weakly curved [31], microporous [15,32–34], and spherical or cylindrical electrodes [35–39]. Analytic approaches have also uncovered effective charge densities that dictate the interactions between curved macroions [40,41]. Some of these more recent geometry-focused investigations are based either on mean-field approaches [32,34,42–44] or on more advanced density functional theory [16,17,39,45–48] and detailed Molecular Dynamics simulations [49–51]. Mean-field approaches are conceptually simple but rely on significant approximations; yet, on a qualitative level, they are often found to describe the behavior of C_{diff} correctly. For instance, Kant and Singh [32] have developed a general analytical theory for the capacitance of an EDL for a wide range of electrode morphology and topology. They demonstrated that the presence of geometrical fluctuations in porous systems entails an enhanced dependence of the differential capacitance on the average pore sizes. Effects of local curvature on the ion distribution near an electrode have been studied by Yang

---

*guilherme.vbossa@outlook.com

[37] by taking into account the interface energy between electrolyte solution and spherical cavities or cylindrical pores. In the regime of small electrostatic potentials, the author reports that the integral capacitance per unit area is dependent on the radius of the cavity (or pore) and independent of the interface energy; for large electrostatic potentials, however, the integral capacitance is dependent only on the interface energy.

Recently, a formalism to compute properties of the EDL as a function of small macroion curvature was proposed for EDL models that apply mean-field electrostatics to *nonideal* equations of state for the ions [52]. The formalism generalizes results derived first by Lekkerkerker [53,54] for the classical Poisson-Boltzmann model, where the underlying equation of state is that of an ideal gas. Examples of frequently used *nonideal* equations of state are the lattice-gas and the Carnahan-Starling equations of state. These equations of state account in an approximate manner for packing effects due to the nonvanishing size of the mobile ions, which becomes important at moderate and large ion concentrations. The same formalism has also been used to calculate the dependence of the differential capacitance C_{diff} on macroion curvature [31], again valid for a continuum description of the ions and an underlying *nonideal* equation of state.

The question arises as to how the predicted curvature dependence of these continuum models compares with molecular simulations that account for the discrete nature and finite size of the ions. The present study represents an attempt to address this question. To this end, we have carried out detailed Monte Carlo simulations for weakly and moderately charged spherical macroions of various radii immersed in an aqueous solution and compared the predicted C_{diff} with two mean-field models that both account approximately for the nonvanishing size of the mobile ions: The first is based on the lattice-gas (LG) equation of state, and the second is based on the Carnahan-Starling (CS) equation of state. Throughout this paper we refer to the two different mean-field approaches as the LG model and the CS model. In the limit of small macroion charge densities, the two mean-field models coincide with the classical Poisson-Boltzmann model. In addition, we show that the quadratic curvature expansion represents an excellent approximation of the full mean-field models (for both the LG model and the CS model) for all macroion sizes and charge densities we have investigated. Our Monte Carlo simulations predict that C_{diff} becomes larger with increasing macroion curvature for small macroion surface charge density and passes through a local minimum with increasing macroion curvature for moderate macroion surface charge density. Most features of simulated behaviors are reproduced qualitatively by our two mean-field models, the LG and CS models. The agreement is best for small macroion surface charge density, where the dependence (but not the absolute value) of C_{diff} on macroion curvature is reproduced almost quantitatively. Overall, our study provides evidence that the quality of mean-field models does not deteriorate when weakly and moderately charged macroions are curved.

II. THEORY

We consider a spherical macroion (or, equivalently, spherical electrode) immersed in an aqueous solution at fixed
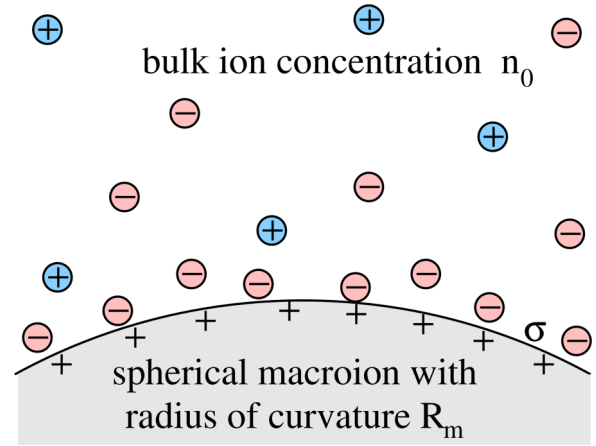
FIG. 1. Schematic illustration of a spherical macroion of radius R_m immersed in a symmetric 1:1 electrolyte: an aqueous solution containing monovalent cations and anions of bulk concentration n_0 each. The macroion carries a uniform surface charge density σ.

temperature T that contains monovalent cations and anions of bulk concentration n_0 and ion volume ν (the same volume for both ion types). The macroion carries a uniform surface charge density σ and has a corresponding electrostatic surface potential Φ_0. Its radius R_m is assumed to be much larger than the size of the ions. In both the mean-field models and the Monte Carlo simulations discussed in this paper, the aqueous solution is modeled as a background of uniform dielectric constant ϵ_w. This is commonly referred to as the primitive model. Figure 1 shows a schematic illustration of the macroion with its adjacent 1:1 electrolyte.

At given R_m, n_0, T, ν, and ϵ_w there will be a fixed relationship between the surface charge density σ and the surface potential Φ_0. The slope of the relationship $\sigma = \sigma(\Phi_0)$ defines the differential capacitance

$$C_{\text{diff}} = \frac{d\sigma}{d\Phi_0}, \qquad (1)$$

which is an experimentally accessible quantity measured in farads per square meter (F/m^2). The manner in which changing the radius R_m of the macroion (or equivalently, its curvature $c = 1/R_m$) affects $C_{\text{diff}} = C_{\text{diff}}(c)$ is the subject of this paper. We shall investigate this question by comparing predictions of different mean-field models with results from Monte Carlo simulations.

Instead of using n_0, ν, and ϵ_w, it is convenient to introduce three characteristic lengths. With the notation e for the elementary charge, ϵ_0 for the vacuum permittivity, and k_B for Boltzmann's constant, the first length is the Bjerrum length, $l_B = e^2/(4\pi\epsilon_0\epsilon_w k_B T)$, the second length is the Debye length, $l_D = (8\pi l_B n_0)^{-1/2}$, and the third length is $l = l_D\sqrt{2n_0\nu}$. Note that only the third length accounts for the nonvanishing ion size. We also define two scaled (dimensionless) surface charge densities, $s = 4\pi l_B l\sigma/e$ and $p = sl_D/(2l) = 2\pi l_B l_D\sigma/e$. The latter is somewhat more convenient to use in models where the ion size is negligible, including the classical Poisson-Boltzmann approach.

A. Mean-field modeling

Our mean-field approach starts from a class of models of the EDL that is characterized by a self-consistency relation [52]

$$l^2 \nabla^2 \Psi = f(\Psi) f'(\Psi), \tag{2}$$

for the dimensionless electrostatic potential $\Psi = e\Phi/k_B T$, where Φ is the electrostatic potential, measured in volts, and ∇^2 denotes the Laplacian. The yet unspecified function

$$f(\Psi) = \sqrt{2 \int_0^\Psi d\bar{\Psi} \tanh \bar{\Psi} \times h^{-1}(2\phi_0 e^{g'(2\phi_0)} \cosh \bar{\Psi})} \tag{3}$$

and its first derivative $f' = f'(\Psi)$ are determined by the underlying equation of state,

$$\frac{P}{k_B T} = 2n_0 \left[1 - \frac{g(\phi)}{\phi} + g'(\phi) \right], \tag{4}$$

of the bulk electrolyte, which describes the pressure P exerted by the anions and cations, both present in the bulk with concentration n_0 and volume fraction $\phi_0 = \nu n_0$ (implying a total volume fraction $\phi = 2\phi_0$ of the anions and cations). The function $g(\phi)$ characterizes the degree of nonideality of the electrolyte. Its first derivative $g'(\phi)$ enters Eq. (3), and so does the inverse h^{-1} of the function $h(\phi) = \phi e^{g'(\phi)}$, defined such that $h^{-1}[h(\phi)] = \phi$.

For example, when modeling the electrolyte as an ideal gas, $P/k_B T = 2n_0$, implying $g(\phi) = 0$ and thus $h(\phi) = \phi$. From Eq. (3) we find $f(\Psi) = 2(l/l_D) \sinh(\Psi/2)$ and its derivative $f'(\Psi) = (l/l_D) \cosh(\Psi/2)$, and finally from Eq. (2) we find the self-consistency relation $l_D^2 \nabla^2 \Psi = \sinh \Psi$. This indeed is the classical Poisson-Boltzmann equation, valid for pointlike ions.

In this paper we focus on two frequently used nonideal equations of state. The first—the LG model—is based on a lattice gas, where cubic cells (each of linear extension $2R$) either are vacant or contain a single (spherical) ion of volume $\nu = 4\pi R^3/3$. The corresponding equation of state for the LG model is

$$\frac{P}{k_B T} = -\frac{\alpha}{\nu} \ln(\alpha - \phi). \tag{5}$$

Here, the factor $\alpha = \pi/6$ accounts for the volume fraction $(4/3)\pi R^3/(2R)^3 = \pi/6$ that a spherical ion of radius R occupies in a cubic cell of size $2R$. From Eq. (5) we deduce the nonideality contribution

$$g(\phi) = \phi(1 - \ln \alpha) + (\alpha - \phi) \ln\left(1 - \frac{\phi}{\alpha}\right) \tag{6}$$

in Eq. (4). The function $h(\phi) = \phi e^{g'(\phi)} = \phi/(\alpha - \phi)$ can be inverted, $h^{-1}(h) = \alpha h/(1 + h)$. From Eq. (3) we then obtain

$$f(\Psi) = \sqrt{2\alpha \ln\left[1 + \frac{2\phi_0}{\alpha}(\cosh \Psi - 1)\right]} \tag{7}$$

and thus the self-consistency relation

$$l^2 \nabla^2 \Psi = \frac{2\phi_0 \sinh \Psi}{1 + \frac{2\phi_0}{\alpha}(\cosh \Psi - 1)}, \tag{8}$$

which has been analyzed extensively in the past, especially for the planar macroion geometry [30,55,56].

The second model that we consider in this paper—the CS model—is based on the Carnahan-Starling equation of state [57–59],

$$\frac{P}{k_B T} = 2n_0 \frac{1 + \phi + \phi^2 - \phi^3}{(1 - \phi)^3}, \tag{9}$$

which predicts the pressure for a system of spherical particles more accurately than the lattice-gas equation of state in Eq. (5). Comparing Eqs. (4) and (9) yields

$$g(\phi) = \phi^2 \frac{4 - 3\phi}{(1 - \phi)^2}. \tag{10}$$

Here, in contrast to Eq. (6), the ensuing function $h(\phi) = \phi e^{g'(\phi)} = \phi \exp[(8\phi - 9\phi^2 + 3\phi^3)/(1 - \phi)^3]$ can only be inverted numerically, preventing us from obtaining an explicit expression of $f(\Psi)$ for the CS model. Nevertheless, we obtain access to the right-hand side of Eq. (2) by computing $f(\Psi)$ and its derivative $f'(\Psi)$ numerically.

For both models, the LG model and the CS model, we have numerically solved the self-consistency relation

$$l^2 \left[\frac{d^2 \Psi}{dr^2} + \frac{2}{r} \frac{d\Psi}{dr} \right] = f(\Psi) f'(\Psi) \tag{11}$$

for our (spherically symmetric) macroion of radius R_m, subject to the boundary conditions $(d\Psi/dr)_{R_m} = -s/l$ and $(d\Psi/dr)_\infty = 0$. From the relationship between the dimensionless surface potential $\Psi_0 = e\Phi_0/k_B T$ and the scaled surface charge density $s = 4\pi l_B l\sigma/e$ we obtain the differential capacitance

$$C_{\text{diff}} = \frac{\epsilon_w \epsilon_0}{l} \frac{ds}{d\Psi_0} \tag{12}$$

as a function of the macroion radius R_m and surface charge density σ.

B. Second-order curvature expansion

As previously discussed [31], we can integrate Eq. (2) for a spherical macroion of sufficiently small curvature $lc \ll 1$ and fixed (scaled) surface charge density s. More specifically, we express the dimensionless surface potential

$$\Psi_0 = f^{-1}(s) - 2 lc \left[\frac{I}{ff'} \right]_{\psi_0 = f^{-1}(s)} + (lc)^2 2 \left[\frac{1}{ff'} \frac{d}{d\psi_0} \left(\frac{I^2}{ff'} \right) \right. $$
$$\left. - \frac{1}{ff'} \int_0^{\psi_0} d\psi \frac{I(\psi)}{f(\psi)} \right]_{\psi_0 = f^{-1}(s)} \tag{13}$$

explicitly as a function of s up to quadratic order in the (scaled) curvature lc. Here, $f = f(\psi_0)$, $f' = f'(\psi_0)$, $I = I(\psi_0) = \int_0^{\psi_0} d\psi f(\psi)$, and f^{-1} is the inverse function of f, defined such that $f[f^{-1}(s)] = s$. Note that the dependence of Ψ_0 on s in Eq. (13) emerges upon calculating both the linear and quadratic term in lc at $\psi_0 = f^{-1}(s)$. That value is identical to the surface potential of a planar macroion. Knowing the surface potential $\Psi_0 = \Psi_0(s)$ of the spherical macroion in

Eq. (13) enables us to calculate the differential capacitance

$$C_{\text{diff}} = \frac{\epsilon_w \epsilon_0}{l} \frac{1}{\frac{d\Psi_0}{ds}} = C_{\text{diff}}^{(0)} \big[1 + 2\tau lc + 2\beta (lc)^2 \big] \quad (14)$$

up to quadratic order in lc, where $C_{\text{diff}}^{(0)}$ is the differential capacitance for a planar macroion ($c = 0$ or, equivalently, $R_m \to \infty$) and where the two constants τ and β describe the first- and second-order dependence of C_{diff} on curvature, respectively. Comparing Eqs. (13) and (14) yields for the differential capacitance of planar geometry $C_{\text{diff}}^{(0)} = \epsilon_w \epsilon_0 f'(\Psi_0)/l$ with $\Psi_0 = f^{-1}(s)$. Hence we arrive at the explicit expression

$$C_{\text{diff}}^{(0)} = \frac{\epsilon_w \epsilon_0}{l} f'[f^{-1}(s)]. \quad (15)$$

In addition, the two constants τ and β in Eq. (14) are given by

$$\tau = \left[\frac{d}{d\psi_0} \left(\frac{I}{ff'} \right) \right]_{\psi_0 = f^{-1}(s)},$$

$$\beta = \left\{ 2 \left[\frac{d}{d\psi_0} \left(\frac{I}{ff'} \right) \right]^2 - \frac{d}{d\psi_0} \left[\frac{1}{ff'} \frac{d}{d\psi_0} \left(\frac{I^2}{ff'} \right) \right] \right.$$
$$\left. + \frac{d}{d\psi_0} \left[\frac{1}{ff'} \int_0^{\psi_0} d\Psi \frac{I(\Psi)}{f(\Psi)} \right] \right\}_{\psi_0 = f^{-1}(s)}. \quad (16)$$

Note that, here again as in Eq. (13), the dependence on s enters by calculating the final expressions at position $\psi_0 = f^{-1}(s)$. Equations (15) and (16) fully characterize the differential capacitance and its dependence on spherical curvature up to second order, subject only to specifying the function $f(\Psi)$ in Eq. (2).

We illustrate the formalism of calculating C_{diff} through a second-order curvature expansion using the classical Poisson-Boltzmann model. As stated above, $g(\phi) = 0$ entails $f(\Psi) = 2(l/l_D)\sinh(\Psi/2)$ and its derivative $f'(\Psi) = (l/l_D)\cosh(\Psi/2)$. To express the surface potential Ψ_0 of a spherical macroion, we also calculate $I(\Psi) = 8(l/l_D)\sinh^2(\Psi/4)$. With that, Eq. (13) reads

$$\Psi_0 = 2\ln(p + q) - l_D c \frac{4(q - 1)}{pq}$$

$$+ (l_D c)^2 \left[\frac{4(q - 1)^2(2q + 1)}{p^3 q^3} - \frac{4\ln\frac{q+1}{2}}{qp} \right], \quad (17)$$

where we recalled $p = sl_D/(2l) = 2\pi l_B l_D \sigma/e$ and introduced the definition $q = \sqrt{p^2 + 1}$. Equation (17) was first derived by Lekkerkerker [53]. Note that, unlike in the LG and CS models, the classical Poisson-Boltzmann model does not account for ion size, implying that the length l becomes meaningless. The relevant length scale in the classical Poisson-Boltzmann model is the Debye length l_D. Indeed, the new scaled curvature $l_D c$ instead of lc appears naturally in Eq. (17). From Eq. (15) we calculate the differential capacitance at planar geometry

$$C_{\text{diff}}^{(0)} = \frac{\epsilon_w \epsilon_0}{l_D} q = \frac{\epsilon_w \epsilon_0}{l_D} \sqrt{1 + \left(2\pi l_B l_D \frac{\sigma}{e} \right)^2}, \quad (18)$$

and from Eqs. (16) we find for the two curvature constants

$$\tau = \frac{l_D}{l} \left[\frac{1}{q^2} - \frac{1}{1 + q} \right],$$

$$\beta = \frac{l_D^2}{l^2} \left[\frac{3q^2 - 2}{q^3(1 + q)} - \frac{1}{q^4(1 + q)^2} - \frac{2q^2 - 1}{q^2(q^2 - 1)} \ln \frac{1 + q}{2} \right], \quad (19)$$

where we recall $(l_D/l)^2 = 1/(2n_0\nu)$. We point out again that because the classical Poisson-Boltzmann theory applies to pointlike ions, the length l (which is the only length scale that reflects the ion volume) must disappear when inserting Eqs. (18) and (19) into Eq. (14). This is indeed the case. Figure 2 shows examples of the relationship between scaled surface charge density $p = sl_D/(2l) = 2\pi l_B l_D \sigma/e$ and surface potential Ψ_0 for different scaled curvatures $l_D c$ according to Eq. (17) [Fig. 2(a)] and the corresponding scaled differential capacitance $C_{\text{diff}} l_D/(\epsilon_w \epsilon_0) = 2(d\Psi_0/dp)^{-1}$ [Fig. 2(b)]. Positive spherical curvature (as illustrated in Fig. 1) somewhat flattens the curve of the differential capacitance (blue and gray curves in Fig. 2) compared with planar geometry (green curve in Fig. 2), where it is given by Eq. (18). Negative spherical curvature (red and black curves in Fig. 2) deepen the V shape of the differential capacitance curves. The dependence of the differential capacitance on spherical curvature for an uncharged surface (at $p = 0$) is simply given by $C_{\text{diff}} = (\epsilon_w \epsilon_0)(1 + l_D c)/l_D$, implying that positive and negative values of $l_D c$ lead to the same positive and negative change, respectively, in C_{diff}.

Usage of the classical Poisson-Boltzmann model is only appropriate when the local ion concentration is sufficiently small everywhere so that steric ion-ion interactions can be neglected. We demonstrate in the Results section that for our parameter choices (especially n_0 and σ) the nonvanishing ion volume ν starts to affect the differential capacitance. This, in fact, defines the regime of moderate surface charge density as opposed to a highly charged macroion, where ion stacking leads to multiple densely packed counterion layers. Hence, rather than considering the classical Poisson-Boltzmann model, we compare our Monte Carlo simulation results with mean-field predictions based on the LG and CS models.

C. Monte Carlo simulations

We have also performed Metropolis Monte Carlo simulations in the canonical ensemble for a 1:1 electrolyte solution of bulk concentration n_0 confined in a neutral impenetrable spherical simulation cell of radius 30 nm. A spherical macroion of radius R_m and uniform surface charge density σ is kept fixed at the center of the simulation cell. The overall electroneutrality of the system is ensured by the addition of neutralizing counterions. Analogously to our previous studies [60–62], we modeled the electrolyte solution within the framework of the primitive model [63], where cations and anions are treated as charged hard spheres of radius $R = (3\nu/4\pi)^{1/3} = 0.2$ nm immersed in a continuous medium of uniform dielectric constant $\epsilon_w = 80$. Thus the electrostatic interaction energy between any two ions i and j is
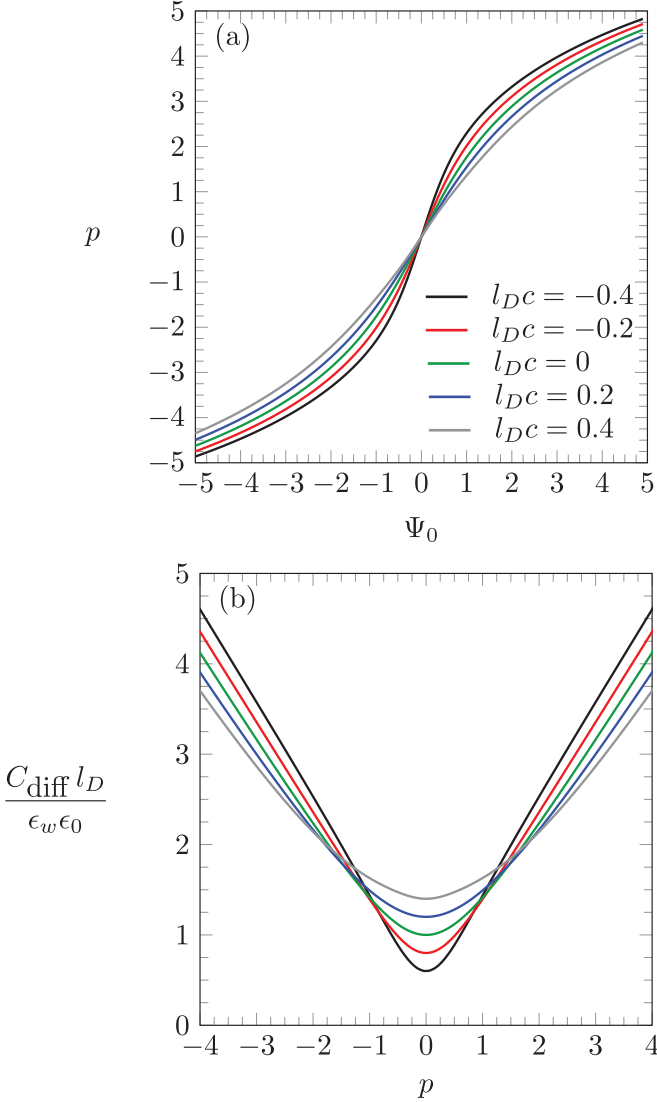
FIG. 2. Predictions of the classical Poisson-Boltzmann model: (a) shows the scaled surface charge density $p = 2\pi l_B l_D \sigma/e$ as a function of the surface potential Ψ_0 calculated according to Eq. (17). In (b), we show the scaled differential capacitance $C_{\text{diff}} l_D/\epsilon_w \epsilon_0$ as a function of $p = 2\pi l_B l_D \sigma/e$. In both plots, different colors indicate different values of the scaled macroion curvature: $l_D c = -0.4$ (black), $l_D c = -0.2$ (red), $l_D c = 0$ (green), $l_D c = 0.2$ (blue), and $l_D c = 0.4$ (gray).

given by

$$\frac{u_{el}(r_{ij})}{k_B T} = \begin{cases} \infty, & r_{ij} < 2R \\ z_i z_j \frac{l_B}{r_{ij}}, & \text{otherwise,} \end{cases} \quad (20)$$

where z_i and z_j are the respective valencies of ions i and j (adopting the values ± 1 in this paper) and r_{ij} is the center-to-center distance between them. The electrostatic interaction energy of a given ion i at distance r_i away from the center of the macroion is

$$\frac{u_{el}(r_i)}{k_B T} = \begin{cases} \infty, & r_i < (R + R_m) \\ 4\pi R_m^2 l_B \frac{\sigma}{e} \frac{z_i}{r_i}, & \text{otherwise.} \end{cases} \quad (21)$$

For each value of σ, our simulations generate the ionic concentrations of cations and anions, n_+ and n_-, respectively. We use the resulting volume charge density $\rho = e(n_+ - n_-)$ to numerically solve the Poisson equation, $\nabla^2 \Psi = -4\pi l_B \rho/e$, and obtain the (scaled) electrostatic potential Ψ anywhere in space. In order to extract the differential capacitance C_{diff}, we first create a list of values (σ, Ψ_0), where Ψ_0 is the average surface potential. Then, we calculate the numerical values of C_{diff} using the algorithm developed by Lamperski and Zydor [64].

III. RESULTS

We have calculated the differential capacitance from Monte Carlo simulations and from two mean-field theories (the LG and CS models), the latter both for numerically solving the self-consistency relation for arbitrary curvature as specified in Eq. (11) and for the small-curvature expansion according to Eq. (14). Throughout this paper, we fix anions and cations of our symmetric 1:1 electrolyte to have a radius $R = 0.2$ nm and bulk concentration $n_0 = 0.056$ nm^{-3} (which is a 0.1 M solution). Together with the dielectric constant of water, $\epsilon_w = 80$, this leads to a Bjerrum length $l_B = 0.7$ nm, a Debye length $l_D = 1$ nm, and $l = 0.061$ nm. The two parameters we vary are the surface charge density σ and radius of the spherical macroion R_m. In our simulations, we have varied the scaled surface charge density $p = 2\pi l_B l_D \sigma/e$ in the range $-1.76 \leqslant p \leqslant 1.76$. For the surface charge density, this corresponds to a maximal magnitude of $|\sigma| = 0.4$ e/nm^2. We have not carried out Monte Carlo simulations beyond that limit.

Figure 3(a) shows the scaled differential capacitance $C_{\text{diff}} l_D/(\epsilon_w \epsilon_0)$ as a function of p. Monte Carlo simulation results are displayed as colored circles; different colors refer to different macroion radii: $R_m = 2$ nm (green), $R_m = 3$ nm (blue), $R_m = 4$ nm (red), $R_m = 5$ nm (black), and the limiting case $R_m \to \infty$ (gray). Corresponding mean-field predictions based on the LG model [i.e., numerical solutions of Eq. (11)] are added as color-matching solid lines.

The results for a planar macroion with $R_m \to \infty$ [the gray circles and gray solid line in Fig. 3(a)] have been presented and discussed in previous work [60–62,65]. Especially for small surface charge densities, the mean-field model prediction overestimates the simulation results. This can be corrected phenomenologically by adding a Stern layer to the mean-field model [65,66]. However, Monte Carlo simulations predict the thickness of the Stern layer to shrink with growing ion size, which is inconsistent with the commonly postulated proportionality of ion size and Stern layer thickness [67]. Qualitative agreement between simulations and mean-field modeling is recovered upon adding short-ranged ion-ion interactions (which represent hydration effects due to the ordering of water molecules near ions) to the Coulomb and excluded volume interaction [60]. In this case, there is no need anymore to add a Stern layer. Hydration-mediated interactions are not accounted for in this paper; we nevertheless find it beneficial to refrain from adding a Stern layer: This exposes the curvature dependence of the mean-field predictions more clearly and discharges us from speculating as to how the Stern layer might behave as a function of macroion curvature. Despite
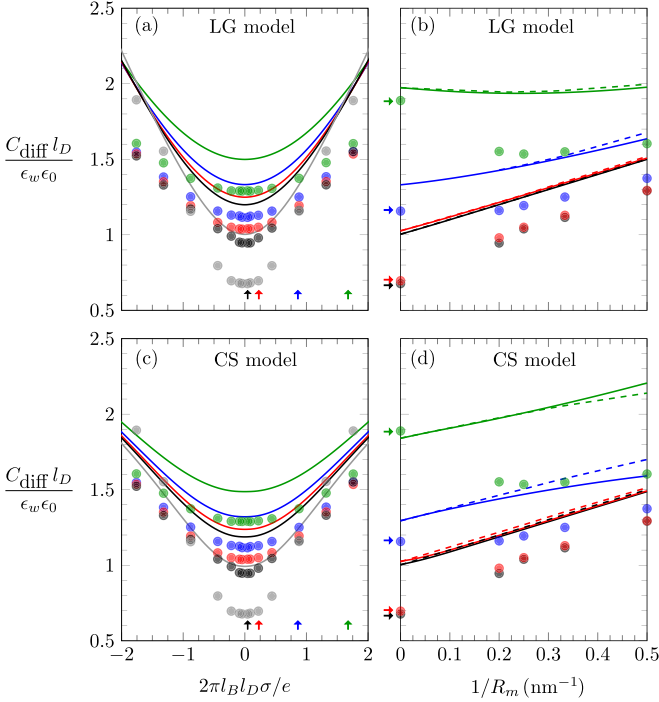
FIG. 3. (a) and (c) Scaled differential capacitance $C_{\mathrm{diff}} l_D / \epsilon_w \epsilon_0$ as a function of scaled surface charge density $p = 2\pi l_B l_D \sigma / e$. Different colors indicate different macroion radii: $R_m = 2$ nm (green), $R_m = 3$ nm (blue), $R_m = 4$ nm (red), $R_m = 5$ nm (black), and the limiting case $R_m \to \infty$ (gray). (a) is for the LG model, and (c) is for the CS model. (b) and (d) Scaled differential capacitance $C_{\mathrm{diff}} l_D / \epsilon_w \epsilon_0$ vs macroion curvature $1/R_m$. Different colors correspond to different values of the surface charge density: $\sigma = 0.01$ e/nm^2 (black), $\sigma = 0.05$ e/nm^2 (red), $\sigma = 0.2$ e/nm^2 (blue), and $\sigma = 0.4$ e/nm^2 (green). (b) is for the LG model, and (d) is for the CS model. In all four plots, circles are predictions obtained from Monte Carlo simulations, and solid lines indicate the results from numerically solving the self-consistency relation in Eq. (11). The dashed lines in (b) and (d) are results from the small-curvature expansion according to Eqs. (14)–(16). The four choices of σ displayed in (b) and (d) are indicated at the bottom of (a) and (c) by small color-matching arrowheads.

the differences between simulation and mean-field results, the planar macroion geometry serves us as a useful reference to investigate the influence of macroion curvature.

Figure 3(a) reveals a growing differential capacitance with increasing curvature for small $|\sigma|$. This increase reflects the larger space available to the ions near the macroion surface, which allows some ions to decrease their distance to the macroion. This stronger condensation implies a larger differential capacitance. Representing the electric double layer by a water-filled spherically curved parallel-plate capacitor with one plate having curvature $1/R_m$ and surface charge density σ and the other plate having curvature $1/(R_m + l_D)$ and surface charge density $\sigma/(1 + l_D/R_m)^2$, we find in the limit $R_m \gg l_D$ the expression

$$C_{\mathrm{diff}} = \epsilon_w \epsilon_0 \left(\frac{1}{l_D} + \frac{1}{R_m} \right), \qquad (22)$$

in agreement with our observation of a growing differential capacitance for the smaller macroions. As already stated above, Eq. (22) is also the correct result of the small-curvature expansion in the Debye-Hückel limit $p \to 0$ [Eqs. (14)–(16) in the limit of vanishingly small surface charge density] for any curvature $c = 1/R_m$. That is, Eq. (22) also results from solving the differential equation $\Psi''(r) + 2\Psi'(r)/r = \Psi(r)/l_D^2$, subject to the boundary conditions $\Psi'(R_m) = -s/l$ and $\Psi(r \to \infty) = 0$, and subsequent calculation of C_{diff} through Eq. (12).

To more clearly discern the dependence of C_{diff} on curvature, we have replotted a subset of the simulation data as a function of curvature $1/R_m$ in Fig. 3(b). The four values for $2\pi l_B l_D \sigma / e$ that we have selected to be displayed are marked near the bottom of Fig. 3(a) by four arrowheads, colored black, red, blue, and green. Figure 3(b) shows Monte Carlo results and corresponding mean-field predictions using the same coloring scheme: $\sigma = 0.01$ e/nm^2 (black), $\sigma = 0.05$ e/nm^2 (red), $\sigma = 0.2$ e/nm^2 (blue), and $\sigma = 0.4$ e/nm^2 (green). Solid lines in Fig. 3(b) account for the full curvature dependence according to Eqs. (11) and (12), and dashed lines represent the small-curvature expansion according to Eqs. (14)–(16). Clearly, apart from the difference between simulations and mean-field predictions that we already observed for planar macroion geometry [60–62], the mean-field model reproduces the curvature dependence of the differential capacitance reasonably well. This applies to both the increase in the differential capacitance with curvature for small $|\sigma|$ [see the black, red, and blue solid lines in Fig. 3(b)] and the local minimum in C_{diff} for larger $|\sigma|$ [see the green solid line in Fig. 3(b)]. The second-order curvature expansion [dashed lines in Fig. 3(b)] accurately reproduces the numerical results from Eq. (11) (the corresponding solid lines) up to the maximal curvature, $1/R_m = 1/(2 \text{ nm})$, used in our simulations.

Figures 3(c) and 3(d) compare our simulation data with the mean-field model that employs the CS equation of state. All parameters and color coding in Figs. 3(c) and 3(d) correspond to our choices in Figs. 3(a) and 3(b); the only difference is the underlying equation of state: Eq. (5) for Figs. 3(a) and 3(b) and Eq. (9) for Figs. 3(c) and 3(d). For small surface charge density ($p \ll 1$), both mean-field models effectively coincide and are also identical to the classical Poisson-Boltzmann model. The underlying reason is that the small value of $\nu n_0 = 0.0019$ renders steric ion-ion interactions in the bulk virtually irrelevant. In the limit $p \to 0$, both mean-field models recover the Debye-Hückel limit according to Eq. (22). Close to that limit, both mean-field models reproduce the curvature-induced changes (but not the absolute value) of C_{diff} almost quantitatively. Differences arise for larger $|p|$, where none of the two mean-field models is able to capture the qualitative features of the observed simulation results. Specifically, at $\sigma = 0.4$ e/nm^2 [the green lines in Figs. 3(b) and 3(d)] the LG model predicts a largely constant C_{diff} and the CS model predicts an increasing C_{diff} as a function of curvature, whereas the Monte Carlo simulations produced an initial decrease.

Our two mean-field models (the LG model and the CS model) make similar predictions for $|p| \lesssim 2$ but deviate substantially for $|p| \gtrsim 2$. Figure 4 compares the differential capacitance of the two models directly for a larger range of $|p|$ than that covered by our simulations: Solid lines
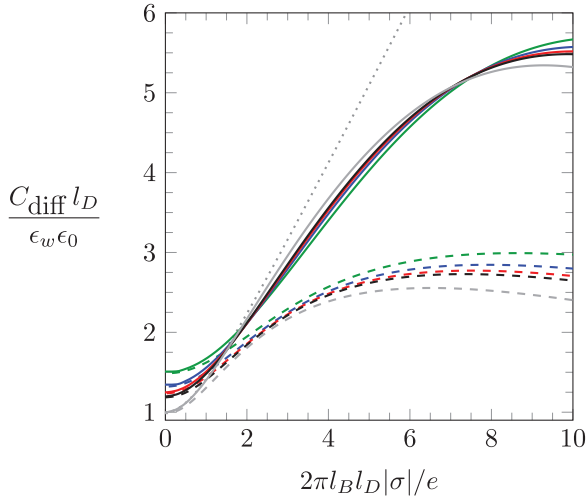
FIG. 4. Scaled differential capacitance $C_{\mathrm{diff}} l_D / \epsilon_w \epsilon_0$ vs scaled surface charge density $|p| = 2\pi l_B l_D |\sigma|/e$ for $R_m = 2$ nm (green), $R_m = 3$ nm (blue), $R_m = 4$ nm (red), $R_m = 5$ nm (black), and the limiting case $R_m \to \infty$ (gray). Solid lines correspond to the LG model, and dashed lines correspond to the CS model, both calculated according to Eq. (11). The dotted gray line is the prediction of the classical Poisson-Boltzmann model for flat geometry ($R_m \to \infty$) according to Eq. (18).

correspond to the LG model, and dashed lines correspond to the CS model. For $|p| \gtrsim 2$, the local ion concentrations close to the macroion surface become large, rendering the differences between the LG and CS equations of state increasingly important and exhibiting the characteristic camel-shape that emerges as a consequence of the counterion stacking near highly charged surfaces [68]. The gray lines correspond to the planar geometry ($R_m \to \infty$). For reference, we have also added the prediction of the classical Poisson-Boltzmann model for flat geometry according to Eq. (18) (dotted gray line). Most notably for a highly charged macroion, the CS model predicts a smaller differential capacitance as compared with the LG model. This can be rationalized by the larger osmotic pressure associated with the CS model, thus pushing the mobile ions closer to the macroion surface [60]. This feature is only weakly modulated by the curvature of the macroion.

In Fig. 5, we display the constants, τ [Fig. 5(a)] and β [Fig. 5(b)], as a function of the scaled surface charge density $|p| = 2\pi l_B l_D |\sigma|/e$. The red dashed lines in each plot correspond to the classical Poisson-Boltzmann model with its analytic expressions in Eq. (19). Already the Poisson-Boltzmann predictions of τ and β as a function of $|p|$ are rather complex, with sign changes and local extrema in both cases. Recall from Eq. (19) that the limit $p = 0$ produces $\tau = l_D/(2l) = 8.20$ and $\beta = 0$, in agreement with Fig. 5. With increasing $|p|$, the constant τ decreases, vanishes for $p = 1.27$, and then adopts the local minimum $\tau = -0.141 \, l_D/l$ at $q = 3.21$. For large $|p| \gg 1$, the constant τ approaches the limit $\tau = 0$. Analogously, with increasing $|p|$ the constant β initially increases, adopts the local maximum $\beta = 0.261 \, l_D^2/l^2$ at $|p| = 0.951$, then (while decreasing) passes through $\beta = 0$ at $|p| = 5.83$, adopts the local minimum $\beta = -0.007\,19 \, l_D^2/l^2$
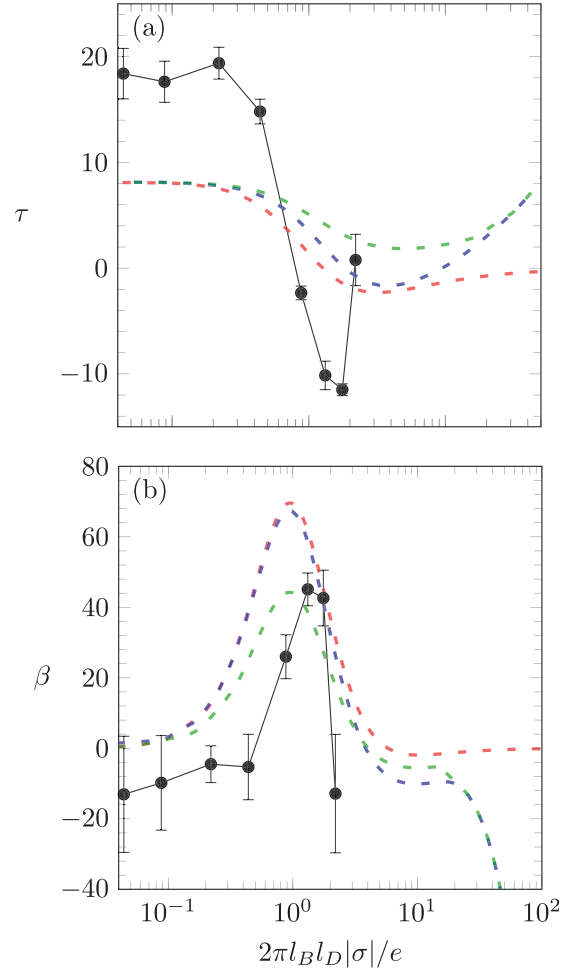
FIG. 5. The constants τ (a) and β (b) as a function of the scaled surface charge density $|p| = 2\pi l_B l_D |\sigma|/e$. Symbols (black circles) are data from Monte Carlo simulations, and dashed lines correspond to mean-field results obtained according to the classical Poisson-Boltzmann theory (red), the LG model (blue), and the CS model (green). The solid lines connecting the black circles serve as a guide to the eye.

at $|p| = 10.24$, and finally approaches the limiting value $\beta = 0$ for $|p| \gg 1$.

Figure 5 also shows predictions from the LG model (blue dashed lines) and from the CS model (green dashed lines). In the Debye-Hückel regime, $|p| \ll 1$, the predictions of all our mean-field models coincide. For growing $|p|$, we observe the same qualitative behavior, namely, a local minimum for τ and a local maximum for β. Qualitative differences emerge in the limit $|p| \gg 1$, where both the LG and CS models converge to the same limiting behavior [31], dictated by the stacking of counterion layers in the vicinity of the highly charged macroion surface. To find the limiting behavior, we consider a spherical macroion of radius $R_m = 1/c$ and charge density $\sigma \geqslant 0$, with a region of counterions of uniform density $-e/v$ inside a spherical shell $R_m < r < R_m + w$ with the shell thickness

$$w = R_m \left[\left(1 + \frac{3v\sigma}{eR_m} \right)^{1/3} - 1 \right]. \tag{23}$$

The potential at the macroion surface $\Phi_0 = \Phi(R_m)$ results from the differential equation $\epsilon_w \epsilon_0 [\Phi''(r) + 2\Phi'(r)/r] = e/v$ subject to the boundary conditions $\epsilon_w \epsilon_0 \Phi'(R_m) = -\sigma$ and $\Phi(R_m + w) = 0$. We find for the differential capacitance

$$C_{\text{diff}} = \frac{d\sigma}{d\Phi_0} = \frac{\epsilon_w \epsilon_0}{R_m \left[1 - \frac{1}{\left(1 + \frac{3v\sigma}{eR_m} \right)^{1/3}} \right]}. \qquad (24)$$

Expanding this result up to quadratic order in c yields

$$C_{\text{diff}} = \epsilon_w \epsilon_0 \left[\frac{e}{v\sigma} + 2c - \frac{2v\sigma}{3e} c^2 \right] \qquad (25)$$

and upon comparison with Eq. (14) thus $\tau = v\sigma/(el) = 2pl/l_D = s$ and $\beta = -(v\sigma/el)^2/3 = (4/3)p^2l^2/l_D^2 = -s^2/3$. This agrees with our findings for the LG and CS models in the limit $|p| \gg 1$ shown in Fig. 5.

Figure 5 also displays an estimate of τ and β from our Monte Carlo simulations (black circles). We have extracted this estimate from Figs. 3(b) and 3(d) by fitting a quadratic function to the first three simulation data points (for $c = 0$, $c = 0.2$ nm^{-1}, and $c = 0.25$ nm^{-1}). Although this estimate suffers from the absence of data points at macroion curvatures $0 < c < 0.25$ nm^{-1}, the qualitative features of τ exhibiting a pronounced local minimum and β passing through a pronounced local maximum appear to be reproduced.

IV. CONCLUSIONS

In this paper, we have compared the predictions for the differential capacitance C_{diff} from Monte Carlo simulations with those from mean-field modeling. In the Monte Carlo simulations we have represented the mobile ions of the electrolyte by hard spheres of radius 0.2 nm and the solvent by a uniform dielectric background. Our goal was to extend the comparison from the planar geometry to spherically curved macroions (of radii from $R_m = 2$ nm to $R_m = 5$ nm) with small and moderate surface charge densities ($|\sigma| \leqslant 0.4$ e/nm^2). Our mean-field models were based on two underlying equations of state, the lattice-gas (LG) and Carnahan-Starling (CS) equations of state, and numerical solutions of the corresponding self-consistency relation. We emphasize that our work systematically compares these modified mean-field models of the EDL with simulations for curved macroions. For small

surface charge densities we find that while our mean-field models overestimate C_{diff}, they accurately reproduce its curvature dependence. The overestimation is related to the absence of a Stern layer, which we have previously discussed in detail for the planar geometry [60–62,65]. For moderate surface charge density, our mean-field models turn less capable to reproduce the qualitative features of the curvature dependence of C_{diff}.

The LG and CS equations of state are members of a class for which we have recently calculated the energy [52] and the differential capacitance [31] of the EDL near weakly curved interfaces (up to quadratic order in curvature). Consequently, we have used the quadratic curvature expansion of C_{diff} and compared it with the full solutions of the self-consistency relation, resulting in excellent agreement for the macroion radii and surface charge densities considered in this paper.

Hence two conclusions emerge from the present work: First, the level of accuracy of mean-field modeling is independent of the macroion radius, at least for small surface charge density of the macroion. Second, the quadratic curvature expansion of C_{diff} for the LG and CS models accurately reproduces the corresponding numerical solutions of the self-consistency relation, which are valid for any curvature. These conclusions are subject to the macroion radii and surface charge densities considered in this paper. Investigations for large curvature (where the radii of curvature approach the ion sizes) and highly charged macroions (where ion stacking takes place), as well as extensions of the present approach via the incorporation of nonelectrostatic interactions—such as solvent-mediated hydration interactions—remain as future projects.

[1] R. Epsztein, E. Shaulsky, M. Qin, and M. Elimelech, Activation behavior for ion permeation in ion-exchange membranes: Role of ion dehydration in selective transport, J. Membr. Sci. **580**, 316 (2019).

[2] P. Shui and E. Alhseinat, Quantitative insight into the effect of ions size and electrodes pores on capacitive deionization performance, Electrochim. Acta **329**, 135176 (2020).

[3] F. Mugele, B. Bera, A. Cavalli, I. Siretanu, A. Maestro, M. Duits, M. Cohen-Stuart, D. van den Ende, I. Stocker, and I. Collins, Ion adsorption-induced wetting transition in oil-water-mineral systems, Sci. Rep. **5**, 10519 (2015).

[4] J. R. Miller and A. F. Burke, Electrochemical capacitors: Challenges and opportunities for real-world applications, Electrochem. Soc. Interface **17**, 53 (2008).

[5] B. E. Conway, *Electrochemical Supercapacitors: Scientific Fundamentals and Technological Applications* (Springer, New York, 2013).

[6] J. Yan, Q. Wang, T. Wei, and Z. Fan, Recent advances in design and fabrication of electrochemical supercapacitors with high energy densities, Adv. Energy Mater. **4**, 1300816 (2014).

[7] P. Simon, Y. Gogotsi, and B. Dunn, Where do batteries end and supercapacitors begin? Science **343**, 1210 (2014).

[8] F. Béguin, V. Presser, A. Balducci, and E. Frackowiak, Carbons and electrolytes for advanced supercapacitors, Adv. Mater. (Weinheim) **26**, 2219 (2014).

[9] K. Brousse, P. Huang, S. Pinaud, M. Respaud, B. Daffos, B. Chaudret, C. Lethien, P.-L. Taberna, and P. Simon, Electrochemical behavior of high performance on-chip porous carbon films for micro-supercapacitors applications in organic electrolytes, J. Power Sources **328**, 520 (2016).

[10] M. Salanne, B. Rotenberg, K. Naoi, K. Kaneko, P.-L. Taberna, C. P. Grey, B. Dunn, and P. Simon, Efficient storage mechanisms for building better supercapacitors, Nat. Energy **1**, 16070 (2016).

[11] R. Burt, K. Breitsprecher, B. Daffos, P.-L. Taberna, P. Simon, G. Birkett, X. Zhao, C. Holm, and M. Salanne, Capacitance of nanoporous carbon-based supercapacitors is a trade-off between the concentration and the separability of the ions, J. Phys. Chem. Lett. **7**, 4015 (2016).

[12] C. Bodin, E. Mourad, D. Zigah, S. Le Vot, S. A. Freunberger, F. Favier, and O. Fontaine, Biredox ionic liquids: New opportunities toward high performance supercapacitors, Faraday Discuss. **206**, 393 (2018).

[13] Z. Li, G. Jeanmairet, T. Méndez-Morales, B. Rotenberg, and M. Salanne, Capacitive performance of water-in-salt electrolytes in supercapacitors: A simulation study, J. Phys. Chem. C **122**, 23917 (2018).

[14] J. Huang, B. G. Sumpter, and V. Meunier, A universal model for nanoporous carbon supercapacitors applicable to diverse pore regimes, carbon materials, and electrolytes, Chem. Eur. J. **14**, 6614 (2008).

[15] H. Wang and L. Pilon, Accurate simulations of electric double layer capacitance of ultramicroelectrodes, J. Phys. Chem. C **115**, 16711 (2011).

[16] E. Paek, A. J. Pak, and G. S. Hwang, Curvature effects on the interfacial capacitance of carbon nanotubes in an ionic liquid, J. Phys. Chem. C **117**, 23539 (2013).

[17] J. Yang, A. Gallegos, C. Lian, S. Deng, H. Liu, and J. Wu, Curvature effects on electric-double-layer capacitance, Chin. J. Chem. Eng. **31**, 145 (2021).

[18] E. H. Lahrar, I. Deroche, C. Matei Ghimbeu, P. Simon, and C. Merlet, Simulations of ionic liquids confined in surface-functionalized nanoporous carbons: Implications for energy storage, ACS Appl. Nano Mater. **4**, 4007 (2021).

[19] Z. Lian, H. Chao, and Z.-G. Wang, Effects of confinement and ion adsorption in ionic liquid supercapacitors with nanoporous electrodes, ACS Nano **15**, 11724 (2021).

[20] S. Kondrat and A. Kornyshev, Superionic state in double-layer capacitors with nanoporous electrodes, J. Phys.: Condens. Matter **23**, 022201 (2010).

[21] P. Simon and Y. Gogotsi, Charge storage mechanism in nanoporous carbons and its consequence for electrical double layer capacitors, Philos. Trans. R. Soc., A **368**, 3457 (2010).

[22] K. Jayaramulu, D. P. Dubal, B. Nagar, V. Ranc, O. Tomanec, M. Petr, K. K. R. Datta, R. Zboril, P. Gómez-Romero, and R. A. Fischer, Ultrathin hierarchical porous carbon nanosheets for high-performance supercapacitors and redox electrolyte energy storage, Adv. Mater. (Weinheim) **30**, 1705789 (2018).

[23] E. Frackowiak and F. Beguin, Carbon materials for the electrochemical storage of energy in capacitors, Carbon **39**, 937 (2001).

[24] A. G. Pandolfo and A. F. Hollenkamp, Carbon properties and their role in supercapacitors, J. Power Sources **157**, 11 (2006).

[25] G. Wang, L. Zhang, and J. Zhang, A review of electrode materials for electrochemical supercapacitors, Chem. Soc. Rev. **41**, 797 (2012).

[26] H. Shao, Y.-C. Wu, Z. Lin, P.-L. Taberna, and P. Simon, Nanoporous carbon for electrochemical capacitive energy storage, Chem. Soc. Rev. **49**, 3005 (2020).

[27] C. Ma, Q. Fan, M. Dirican, N. Subjalearndee, H. Cheng, J. Li, Y. Song, J. Shi, and X. Zhang, Rational design of meso-/micropores for enhancing ion transportation in highly-porous carbon nanofibers used as electrode for supercapacitors, Appl. Surf. Sci. **545**, 148933 (2021).

[28] R. Pal, S. L. Goyal, I. Rawal, A. K. Gupta, and Ruchi, Efficient energy storage performance of electrochemical supercapacitors based on polyaniline/graphene nanocomposite electrodes, J. Phys. Chem. Solids **154**, 110057 (2021).

[29] V. Lockett, M. Horne, R. Sedev, T. Rodopoulos, and J. Ralston, Differential capacitance of the double layer at the electrode/ionic liquids interface, Phys. Chem. Chem. Phys. **12**, 12499 (2010).

[30] K. Bohinc, G. V. Bossa, and S. May, Incorporation of ion and solvent structure into mean-field modeling of the electric double layer, Adv. Colloid Interface Sci. **249**, 220 (2017).

[31] G. V. Bossa, R. Downing, J. Abrams, B. K. Berntson, and S. May, Differential capacitance of electrolytes at weakly curved electrodes, J. Phys. Chem. C **123**, 1127 (2018).

[32] R. Kant and M. B. Singh, Generalization of the Gouy-Chapman-Stern model of an electric double layer for a morphologically complex electrode: Deterministic and stochastic morphologies, Phys. Rev. E **88**, 052303 (2013).

[33] S. Kondrat and A. Kornyshev, Charging dynamics and optimization of nanoporous supercapacitors, J. Phys. Chem. C **117**, 12399 (2013).

[34] A. A. Lee, S. Kondrat, and A. A. Kornyshev, Single-File Charge Storage in Conducting Nanopores, Phys. Rev. Lett. **113**, 048701 (2014).

[35] M. C. Henstridge, E. J. Dickinson, and R. G. Compton, On the estimation of the diffuse double layer of carbon nanotubes using classical theory: Curvature effects on the gouy–chapman limit, Chem. Phys. Lett. **485**, 167 (2010).

[36] H. Wang, J. Varghese, and L. Pilon, Simulation of electric double layer capacitors with mesoporous electrodes: Effects of morphology and electrolyte permittivity, Electrochim. Acta **56**, 6189 (2011).

[37] F. Yang, Size effect on electric-double-layer capacitances of conducting structures, Phys. Lett. A **383**, 2353 (2019).

[38] M. Janssen, Curvature affects electrolyte relaxation: Studies of spherical and cylindrical electrodes, Phys. Rev. E **100**, 042602 (2019).

[39] M. Abareghi and E. Keshavarzi, Diffuse and stern capacitances at the concave wall of spherical cavities by density functional theory, J. Electroanal. Chem. **883**, 115060 (2021).

[40] L. Šamaj and E. Trizac, Effective charge of cylindrical and spherical colloids immersed in an electrolyte: The quasi-planar limit, J. Phys. A: Math. Theor. **48**, 265003 (2015).

[41] L. Šamaj and E. Trizac, Electric double layers with surface charge modulations: Exact Poisson-Boltzmann solutions, Phys. Rev. E **100**, 042611 (2019).

[42] E. J. Dickinson and R. G. Compton, Diffuse double layer at nanoelectrodes, J. Phys. Chem. C **113**, 17585 (2009).

[43] J. Varghese, H. Wang, and L. Pilon, Simulating electric double layer capacitance of mesoporous electrodes with cylindrical pores, J. Electrochem. Soc. **158**, A1106 (2011).

[44] A. Reindl, M. Bier, and S. Dietrich, Electrolyte solutions at curved electrodes. I. Mesoscopic approach, J. Chem. Phys. **146**, 154703 (2017).

[45] J. Huang, B. G. Sumpter, and V. Meunier, Theoretical model for nanoporous carbon supercapacitors, Angew. Chem., Int. Ed. **47**, 520 (2008).

[46] A. Reindl, M. Bier, and S. Dietrich, Electrolyte solutions at curved electrodes. II. Microscopic approach, J. Chem. Phys. **146**, 154704 (2017).

[47] T. Yumura, M. Ishikura, and K. Urita, Why pore width of nanoporous carbon materials determines the preferred solvated states of alkaline cations: A density functional theory calculation study, J. Phys. Chem. C **123**, 21457 (2019).

[48] E. Keshavarzi and S. Safdaar, Ionic competition over adsorption into charged spherical cavities affecting the shape of electric double layer capacitance curve and zeta potential: A density functional theory study, J. Electrochem. Soc. **168**, 060535 (2021).

[49] Z. Bo, C. Li, H. Yang, K. Ostrikov, J. Yan, and K. Cen, Design of supercapacitor electrodes using molecular dynamics simulations, Nano-Micro Lett. **10**, 33 (2018).

[50] M. Biagooi and S. N. Oskoee, The effects of slit-pore geometry on capacitive properties: A molecular dynamics study, Sci. Rep. **10**, 6533 (2020).

[51] J. Seebeck, P. Schiffels, S. Schweizer, J.-R. Hill, and R. H. Meißner, Electrical double layer capacitance of curved graphite electrodes, J. Phys. Chem. C **124**, 5515 (2020).

[52] G. V. Bossa, B. K. Berntson, and S. May, Curvature Elasticity of the Electric Double Layer, Phys. Rev. Lett. **120**, 215502 (2018).

[53] H. Lekkerkerker, Contribution of the electric double layer to the curvature elasticity of charged amphiphilic monolayers, Phys. A (Amsterdam) **159**, 319 (1989).

[54] H. Lekkerkerker, The electric contribution to the curvature elastic moduli of charged fluid interfaces, Phys. A (Amsterdam) **167**, 384 (1990).

[55] I. Borukhov, D. Andelman, and H. Orland, Steric Effects in Electrolytes: A Modified Poisson-Boltzmann Equation, Phys. Rev. Lett. **79**, 435 (1997).

[56] Y. Nakayama and D. Andelman, Differential capacitance of the electric double layer: The interplay between ion finite size and dielectric decrement, J. Chem. Phys. **142**, 044706 (2015).

[57] N. F. Carnahan and K. E. Starling, Equation of state for nonattracting rigid spheres, J. Chem. Phys. **51**, 635 (1969).

[58] T. Boublík, Hard-sphere equation of state, J. Chem. Phys. **53**, 471 (1970).

[59] G. Mansoori, N. Carnahan, K. Starling, and T. Leland Jr, Equilibrium thermodynamic properties of the mixture of hard spheres, J. Chem. Phys. **54**, 1523 (1971).

[60] D. L. Z. Caetano, G. V. Bossa, V. M. de Oliveira, M. A. Brown, S. J. de Carvalho, and S. May, Role of ion hydration for the differential capacitance of an electric double layer, Phys. Chem. Chem. Phys. **18**, 27796 (2016).

[61] D. L. Z. Caetano, G. V. Bossa, V. M. de Oliveira, M. A. Brown, S. J. de Carvalho, and S. May, Differential capacitance of an electric double layer with asymmetric solvent-mediated interactions: Mean-field theory and Monte Carlo simulations, Phys. Chem. Chem. Phys. **19**, 23971 (2017).

[62] G. V. Bossa, D. L. Z. Caetano, S. J. de Carvalho, and S. May, Differential capacitance of an electrical double layer with asymmetric ion sizes in the presence of hydration interactions, Electrochim. Acta **321**, 134655 (2019).

[63] T. L. Hill, *An Introduction to Statistical Thermodynamics* (Courier, North Chelmsford, MA, 2012).

[64] S. Lamperski and A. Zydor, Monte Carlo study of the electrode|solvent primitive model electrolyte interface, Electrochim. Acta **52**, 2429 (2007).

[65] G. V. Bossa, D. L. Caetano, S. J. de Carvalho, K. Bohinc, and S. May, Modeling the camel-to-bell shape transition of the differential capacitance using mean-field theory and Monte Carlo simulations, Eur. Phys. J. E: Soft Matter Biol. Phys. **41**, 113 (2018).

[66] L. Daniels, M. Scott, and Z. Mišković, The role of Stern layer in the interplay of dielectric saturation and ion steric effects for the capacitance of graphene in aqueous electrolytes, J. Chem. Phys. **146**, 094101 (2017).

[67] O. Stern, Zur theorie der elektrolytischen doppelschicht, Z. Elektrochem. Angew. Phys. Chem. **30**, 508 (1924).

[68] M. S. Kilic, M. Z. Bazant, and A. Ajdari, Steric effects in the dynamics of electrolytes at large applied voltages. I. Double-layer charging, Phys. Rev. E **75**, 021502 (2007).